




Environmentally friendly *p*-type CTS-based thin-film thermoelectric generator

Tanguy Bernard¹, Marcelo Augusto Malagutti¹, Ketan Lohani¹, Mirco D’Incau¹, Narges Ataollahi¹, and Paolo Scardi^{1,*} 

¹ Department of Civil, Environmental and Mechanical Engineering, University of Trento, Via Mesiano 77, 38123 Trento, Italy

Received: 30 April 2024

Accepted: 6 August 2024

Published online:
22 August 2024

© The Author(s), 2024

ABSTRACT

Cu-based sulphides are promising materials for environmentally friendly Te-free thermoelectric generators (TEGs). Cu₂SnS₃ (CTS) stands out for its electronic properties, stemming from its conductive Cu–S networks, especially in fully disordered cubic structural form. While wet chemical techniques are the most utilized for CTS synthesis, they introduce organic contaminants that reduce electronic connectivity between grains, limiting their performance as in-plane thin-film TEGs. We present a new method to improve the electronic properties of CTS thin films for thermoelectric applications involving three-step dry route synthesis of ball milling, thermal evaporation, and sulfurization of Cu₂–Sn metallic precursors. Via this method, charge carrier concentration increased significantly, as estimated by Hall effect analysis, which was attributed to the Cu-poor stoichiometry, also confirmed via energy-dispersive X-ray spectroscopy (EDXS). Microstructural analysis by scanning electron microscopy (SEM) revealed micrometre-sized grains composed of even smaller crystalline domains, which X-ray diffraction (XRD) showed to be ~ 50 nm in diameter. When compared with literature results, our procedure leads to a fourfold enhancement in the thermoelectric power factor ($PF = S^2\sigma$), determined through the Seebeck coefficient measurements (S) and electronic conductivity (σ) estimated by the van der Pauw technique. The CTS TEG has a power volume density of 2.3 $\mu\text{W K}^{-1} \text{cm}^{-3}$, measured by a custom current–voltage–power (I–V–P) setup with varying load resistance. Results present a 100% increase in performance compared to ink-based techniques and were reproducible across three different batches. This strategy, improving the density of the CTS thin films, offers a new way to enhance Cu-based thin-film TEGs.

Handling Editor: Naiqin Zhao.

Address correspondence to E-mail: paolo.scardi@unitn.it

<https://doi.org/10.1007/s10853-024-10104-w>

Introduction

Thermoelectric generators (TEGs) are energy conversion devices exploiting the Seebeck effect to transform heat into electrical power. Typically constructed using both *p*- and *n*-type semiconductors, these generators are interconnected in series and configured in a π -type geometry to form a TEG module. These modules are then combined to form the commercially available TEGs, covering a larger surface area. Various applications are given to these TEGs in the industry and electronic productive sectors. For the former, more than 60% of the primary energy is lost as residual heat [1] and thermoelectric devices are considered one of the most powerful ways to harvest this form of energy. For the latter, the absence of moving components, silent operation, lack of vibration, and high reliability, make the TEGs compact and with a low maintenance cost [2, 3], therefore being envisaged in sensor applications as well as for powering devices for the Internet of Things [4].

The efficiency of the heat-to-electric energy transformation of a TEG is proportional to its figure of merit, defined as $zT = \frac{S^2\sigma}{\kappa}T$, where S is the Seebeck coefficient, σ is the electrical conductivity, T the absolute temperature, and κ is the thermal conductivity, which is composed of a lattice (κ_l) and electronic (κ_e) contributions ($\kappa = \kappa_l + \kappa_e$). However, the electronic properties (S and σ) are interconnected, i.e. the increase in one generally induces a decrease in the other during material optimization [5]. One of the ways to decouple these two properties is via intrinsic or extrinsic doping. Alternatively, suppressing the lattice component of thermal conductivity proves to be effective, as it does not impact other transport parameters. This can be achieved by nanostructuring, providing obstacles to phonon wave propagation without a significant effect on the electronic conduction, leading to the so-called phonon-glass electron crystal (PGEC) behaviour [5, 6]. In addition, since heat propagation is mainly governed by κ_l , an effective approach for reducing κ is producing thin-film materials such that phonons with wavelengths larger than the thin-film thickness are eliminated [2, 7]. When the substrate is several orders of magnitude larger than the thin film, it is responsible for most of the heat conduction, so the performance of thin-film TEGs is only determined by the improvement of the electrical properties in the power factor, $PF = S^2\sigma = S^2/\rho$, where ρ is the electrical resistivity.

A reduction in thickness offers additional opportunities in microdevice applications such as micro-TEGs [8, 9], micro-coolers [10, 11], and microsensors [12]. However, even if TEGs and micro-TEGs are used in many applications, their commercialization is still limited because of their relatively high costs, estimated at 2000–15000 €/kW [13]. This is mainly due to the use of expensive, rare, and toxic materials based on Te, Bi, Pb, Sb, Ge, Ga, etc. [2, 14]. A widespread development of TEGs can be based on earth-abundant, sustainable, non-toxic, and low-cost materials such as the Cu-based sulphides: Cu₂ZnSnS₄ (CZTS), Cu₂ZnSnSe₄ (CZTSe), CuFeS₂ (CFS), and Cu₂SnS₃ (CTS) [2, 15–18]. Improvement of their electronic conversion has already been proved possible by doping [5], resulting in a significant increase in charge carrier concentration (n).

Among the sulphide-based materials, the best overall performance is given by Cu₂SnS₃ (CTS), as thoroughly discussed in Ref. [19]. It is shown that the electronic properties of CTS are boosted in the disordered cubic form, where cations occupy random positions in the lattice sites. This is responsible for increasing the charge carrier concentration, acting also as phonon scatterers, enhancing both PF and κ [18]. Thin films of CTS have been produced by ink-based techniques [2], sol-gel methods [20], hot injection [21], electron beam deposition followed by sulfurization [22], ultrasonic spray pyrolysis [23], and sulfurized direct current (DC) [24] and radio-frequency (RF) magnetron sputtered Cu₂Sn [25, 26]. However, only Refs. [2, 21] used CTS for TEG fabrication. In addition, as far as we know, the thermal evaporation of CTS has only been explored by Oszoy et al. [27]. Thermal evaporation has the advantage of being a relatively inexpensive technique, with a high deposition rate compared to sputtering techniques. It is a dry route, easily manageable and scalable at an industrial level and generally provides a more homogeneous and dense film compared to ink-based or wet chemistry techniques. For the latter, organic compounds can be trapped between the CTS grains, decreasing the density of the film, and worsening the electrical connection between the grains [28].

In this work, we show the material synthesis and production of TEGs using CTS fabricated via a three-step synthesis involving the use of ball milling (BM), thermal evaporation, and sulfurization of the Cu₂–Sn metallic precursors. Scanning electron microscopy (SEM), X-ray diffraction (XRD), and energy-dispersive X-ray spectroscopy (EDXS) were

used for a thorough structural and morphological characterization. The films were about 1.5 μm in thickness, composed of nanometric domain sizes, with a homogeneous chemical composition. TE characterization based on Seebeck measurements and electronic properties, estimated via the Hall effect approach in van der Pauw geometry, showed that a Cu-poor stoichiometry leads to a three order of magnitude boost in the carrier concentration. The power output of the TEGs was assessed by current–voltage–power (I–V–P) curves, using a specially developed setup for varying load resistance. The obtained results from this method demonstrate that the performance of CTS TEG has enhanced by double as compared with the CTS TEG based on ink deposition [2]. In addition, the use of high-energy ball milling to make the metallic precursor powder (Cu–Sn) avoid the use of stacked thermal evaporation of Cu and Sn powder. This technique allows us to improve the CTS thin-film layer density increasing the overall thermoelectrical performances, which can be easily applied for large scale production of thermoelectric devices and aims to provide a new, solvent-free method for the fabrication of CTS-based TEGs [2].

Experimental details

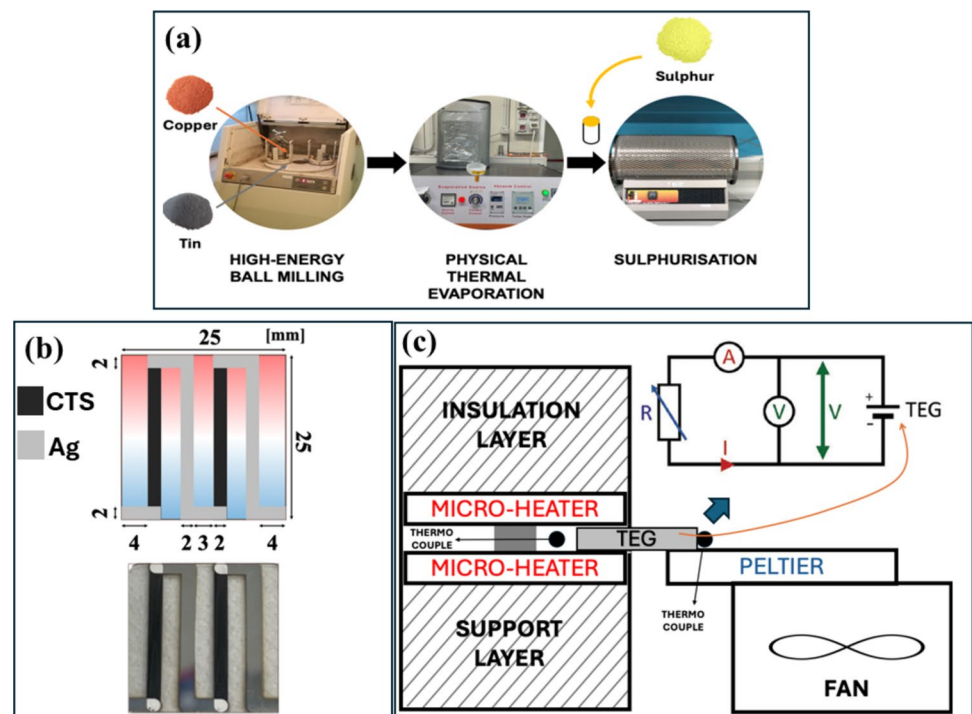
CTS synthesis

Thin-film CTS were prepared employing a novel method consisting of BM of the metallic precursors ($\text{Cu}_2\text{-Sn}$), physical vapour deposition (PVD) via thermal evaporation, and sulfurization of the $\text{Cu}_2\text{-Sn}$ films, sketched in Fig. 1a.

$\text{Cu}_2\text{-Sn}$ powders were produced by high-energy BM of the elementary powders of Cu (Sigma-Aldrich, 99.9%) and Sn (Sigma-Aldrich, 99.8%) using a Fritsch P4 planetary ball mill. Firstly, the Cu and Sn powders were placed in WC vials (80 mL of volume) together with 27 WC balls (12 mm diameter), milled with a ball-to-powder ratio of 100:1. Ethanol (Sigma-Aldrich, 99.9%) was added as a lubricant, corresponding to 10% of the mass of the powder. The main disc rotation was set to 310 rpm, with a -1.80 main disc-to-planet ratio, taking 3 h to complete.

Before the deposition of the $\text{Cu}_2\text{-Sn}$ thin films, the soda-lime-glass (SLG) (dimensions of $25 \times 25 \times 1$ mm) was previously etched using a mixture of KOH and ethanol solution, being further sonicated for 15 min. The substrates were later cleaned with commercial soap and rinsed with ultra-pure water. Subsequently, the $\text{Cu}_2\text{-Sn}$ thin films were deposited using a Tecum

Figure 1 **a** Three-step CTS synthesis method. **b** Schematic diagram of the CTS TEG with the chosen dimensions and the fabricated CTS TEG. **c** Schematic diagram of I–V measurement setup used for the analysis and of the electrical circuit of the I–V measurement setup.



AG VCM600 V1 thermal evaporator. The TEGs were shaped using a stainless-steel shadow mask during the deposition, consisting of two legs with the dimensions provided in Fig. 1b. This procedure was performed in a vacuum at a constant pressure of 5.0×10^{-6} mbar, with an output current of 105 A and voltage of 12 V for 10 min.

The sulfurization of the Cu₂–Sn thin film resulted in the formation of the CTS. The sulfurization process employed a tubular furnace (Carbonite Gero, Sheffield, UK), where the Cu₂–Sn thin films, sided by 50 mg of S (Sigma-Aldrich, 99.5%), were submitted to a 425 °C isothermal for 1 h (heating ramp of 20 °C min⁻¹) under flowing of N₂ gas. The two CTS legs were then connected in series using Ag thin film, deposited from the evaporation of Ag pallets (Kurt J. Lesker, 99.99%, 1/8" Diameter × 1/8" Long). The visual quality of the films and the dimensions of the TEG can be inspected Fig. 1b.

CTS characterization

The XRD measurements have been conducted using a D8 Discover diffractometer (Bruker AXS GmbH) equipped with a Co-K α radiation source with a wavelength of 1.789 Å. A 192 microstrips channels position sensitive detector was employed in a 1D configuration, in θ – 2θ geometry. The data were obtained from 2θ initiating at 15° up to 95°, with a time interval of 1s and a step size of 0.05°. Phase identification was conducted utilizing the PDF4+ database [29]. Rietveld refinement and whole powder pattern analysis were performed using TOPAS7 software [30].

The morphology of the films was characterized via SEM micrographs, obtained with a JSM-7001F FEG-SEM (JEOL, Tokyo, Japan) instrument equipped with an energy-dispersive X-ray spectroscopy detector (EDXS, Oxford INCA PentaFETx3, Oxford, UK). The electron beam energy was in the range of 10–15 keV, with a working distance of 5–10 mm. In addition, the surface profile of the thin film was measured using a Dektak3 Stylus Profilometer (Veeco Instruments, Plainview, NY, USA) equipped with a diamond stylus of 12 μ m radius with a vertical resolution of 10 Å.

Measurements of resistivity, carrier concentration and mobility were carried out via Hall effect measurements in van der Pauw configuration employing a Linseis HCS-1 instrument. A specifically shaped CTS thin film, with dimensions of 12.5 × 12.5 mm, was fabricated to perform the electrical characterization. The

measurement has been carried out in an N₂ atmosphere with a temperature ranging from 303 to 473 K. The Seebeck measurements were realized with the same equipment, using the Seebeck option, with a sample of 20 × 5 mm.

Thermoelectric generator setup

The performance of the TEG was evaluated using a current–voltage (I–V) measurement setup placed in an Ar atmosphere to avoid film oxidation. It is composed of two thermocouples, two micro-heaters for the hot side, and a Peltier cooler connected to a fan for the cold side, as sketched in Fig. 1c. During the generation of a temperature gradient (ΔT) by the micro-heaters, a load resistance placed in series with the TEG varied from 0 to 2 M Ω , by means of a newly developed automated system. The voltage (V) and current (I) were measured with a Keithley 2601 A source meter, simultaneously connected in parallel and in series as shown in the circuit sketched in Fig. 1c. The power output has been evaluated by means of the following standard law: $P_{\text{OUT}} = V \times I = R \times I^2$.

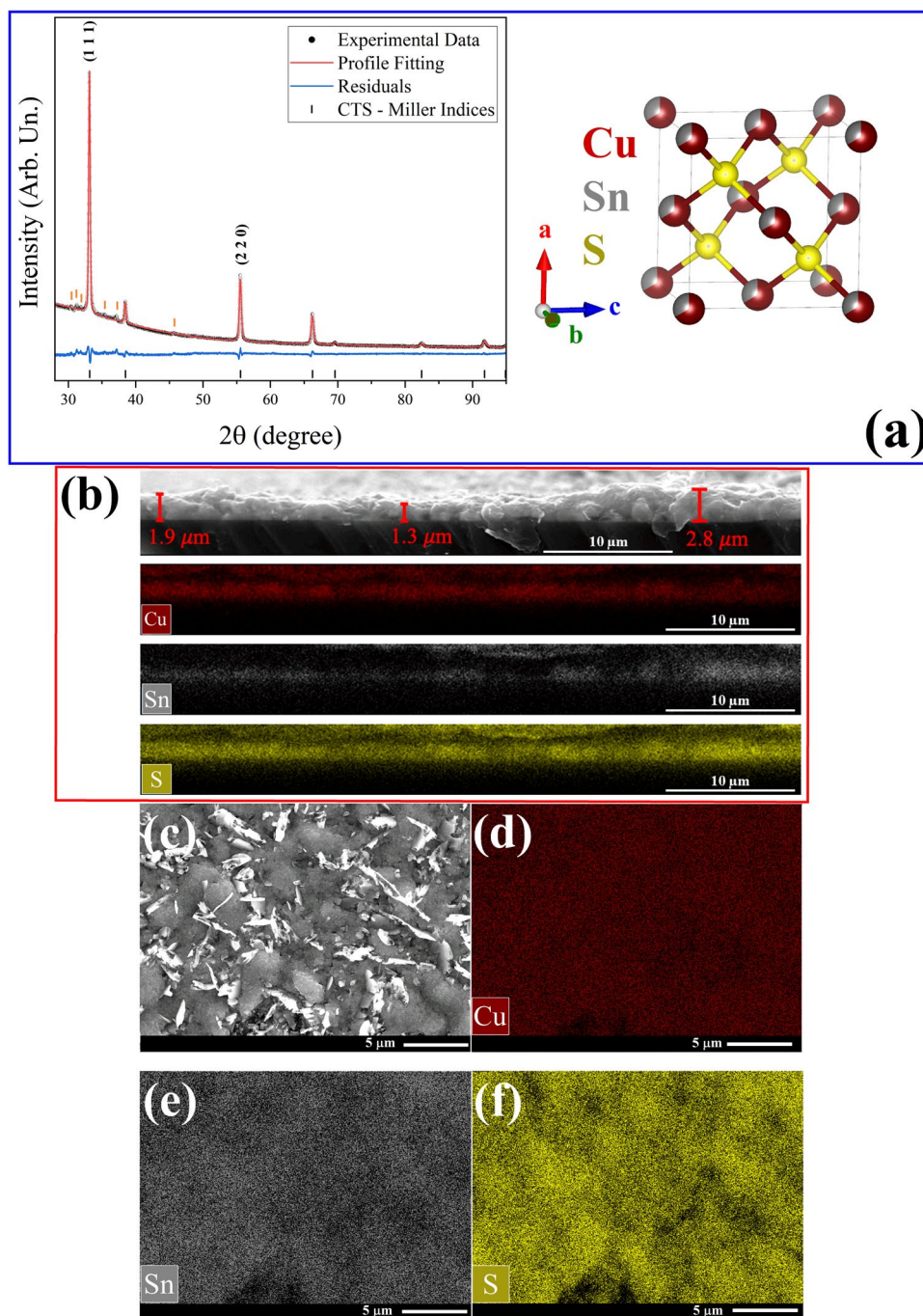
Results and discussion

Material characterization

XRD measurements, as shown in Fig. 2a, can assess the purity of the CTS films. The structure identified is that of a cubic phase, space group $F-43m$ (ICDD-PDF card number 01-089-2877), represented in the inset of the figure. Impurity peaks are marked as orange lines; however, their intensity is insignificant, meaning that their phase percentage in the sample is also low. The Rietveld refinement resulted in a R_{wp} of 3.79%, with a refined lattice parameter of 5.4297(4) Å and preferred orientation along [111] and [220] directions. Microstructural analysis revealed an average crystallite size of 49.7(3) nm, with a microstrain (ϵ_0) of 0.056%.

The surface profile was measured at different positions in the sample using the profilometer, resulting in an average thickness of 1.5 μ m. SEM cross-sectional area measurements of Fig. 2b show a comparable thickness. In addition, the chemical maps revealed a homogeneous distribution of Cu, Sn, and S throughout the film thickness (Fig. 2b). The variation on the EDXS intensities in the chemical map for every element is proportional to the stoichiometry balance of

Figure 2 **a** XRD measurements of the CTS film. The black dots represent the experimental data, the red line represents the Rietveld profile modelling, and the blue line the residuals. The black tick markers represent the Bragg position of the CTS structure and the orange tick markers the impurity phase. **b** Cross section of the CTS thin film. **c–f** Surface scan and chemical maps of CTS thin-film for Cu, Sn, and S in order.



the Cu_2SnS_3 phase elements. Surface morphology is shown by the SEM micrographs of Fig. 2c. The films are made of micrometre-sized grains with a nanometre-scale subgrain structure (~ 50 nm), surrounded by plate-like features. These subgrains are shown in Supplementary Information, Figure S1, and are comparable to the coherent scattering domains observed via XRD line profile analysis. The chemical maps revealed

a homogeneous distribution of the elements throughout the film surface, as depicted in Fig. 2d–f. EDXS revealed that the Cu:Sn ratio is 1.69:1 and the S:Sn ratio is 2.78:1, being Cu and S poor. However, by analysing the pristine $\text{Cu}_2\text{-Sn}$ films (see Figure S2 and Figure S3 for EDXS), we observe that this imbalance in stoichiometry is happening after the sulfurization since the pristine $\text{Cu}_2\text{-Sn}$ thin films were stoichiometric and

homogeneous. The XRD also showed that the pristine $\text{Cu}_2\text{-Sn}$ film is composed of CuSn and Cu_3Sn phases shown in Figure S 4 in a Cu:Sn ratio of 2:1. For the CTS film, the Cu:Sn ratio of 1.69:1 ratio is similar to what was reported by Ozsoy et al. [27] using thermal evaporation of stacked Cu and Sn layers followed by sulfurization [27]. The morphology of CTS samples presented here is also similar to materials synthesized using DC and RF magnetron sputtering and sulfurization [25], proving to be a characteristic of PVD techniques.

The charge carrier concentration (n) of the CTS film is plotted in Fig. 3a. Carrier concentration is three orders of magnitude higher compared to bulk CTS synthesized via solid-state reaction [31–33]. Further evidence of the effect of the Cu-poor stoichiometry on n is found for CTS thin films fabricated via the sol-gel method [34], which presents a similar stoichiometry and also shows a three order of magnitude higher carrier concentration. In addition, it can be seen that n decreases with the temperature, in agreement with the previously cited works [31–34].

Carrier mobility (μ) is presented in Fig. 3a. The mobility is two orders of magnitude lower than bulk stoichiometric CTS [18]. Since the electrical conductivity is given by the known formula:

$$\sigma = n \cdot e \cdot \mu \quad (1)$$

where e is the electron charge, the three-order increase in n is compensated by the two-order decrease in μ , returning an overall one order of magnitude higher σ compared to the pristine CTS [18]. In addition, the Cu-poor stoichiometry present in our case

stabilizes the cubic CTS phase, contrary to Cu-rich materials, which reported a simultaneous presence of tetragonal, monoclinic, and cubic phases for both bulk and thin-film samples [22, 23, 33].

The temperature evolution of the resistivity measured using a van der Pauw configuration is given in Fig. 4a. At ~ 400 K there is a subtle change from non-degenerate to degenerate semiconducting behaviour with temperature, similar to Zhao et al. [35] and Lohani et al. [5] reports. This trend can be explained by the change of behaviour of n and μ at a similar temperature range, since ρ is the inverse of the conductivity, which is proportional to n and μ (Eq. (1)) [details in Figure S10 in Supplementary Note3]. These change in trend at ~ 400 K could be partly attributed to the thermal excitation of the bipolarons [36]. The overall resistivity is lower by one order of magnitude than the stoichiometric high-density CTS bulk samples [33] and similar to Cu-poor CTS thin films made via ultrasonic spray pyrolysis [23, 37], thermal evaporation [27], and sputtering [25]. It can be concluded that the unbalanced stoichiometry of the CTS thin film is beneficial for its conducting properties.

Seebeck values with temperature are shown in Fig. 4a, presenting a linear increase with temperature. However, the overall Seebeck values are two to three times lower than stoichiometric CTS bulk materials [5, 18, 32, 35, 36, 38]. The Cu-poor stoichiometry of the thin films can again explain this effect as it boosts n by three orders of magnitude compared to pristine CTS [39], while the effective mass of the charge carriers (m^*) does not change significantly (Fig. 3b), decreasing

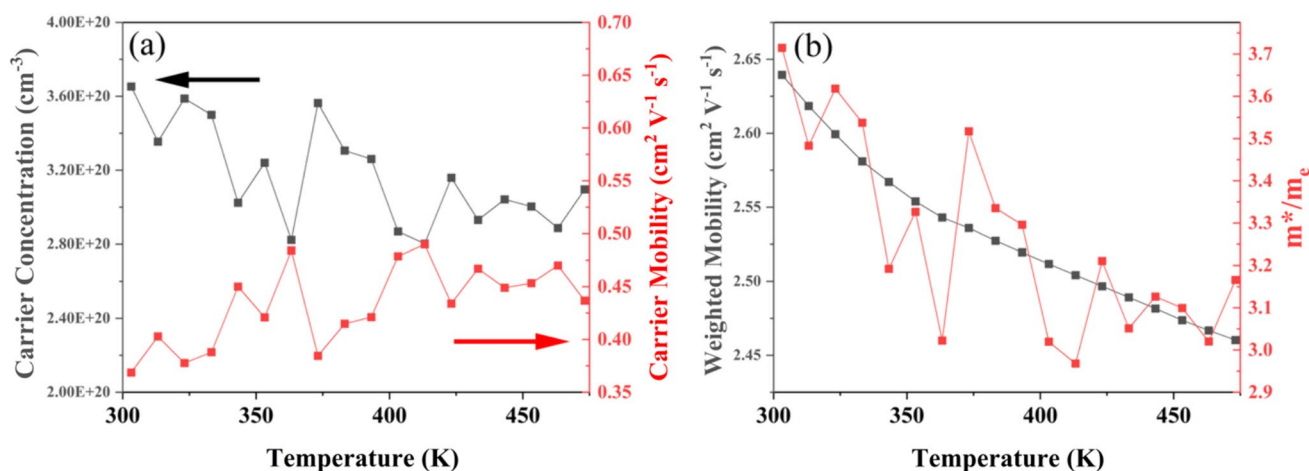


Figure 3 **a** Carrier concentration (left axis) and mobility (right axis). **b** Weighted mobility (left axis) and normalized effective mass of the charge carriers (right axis).

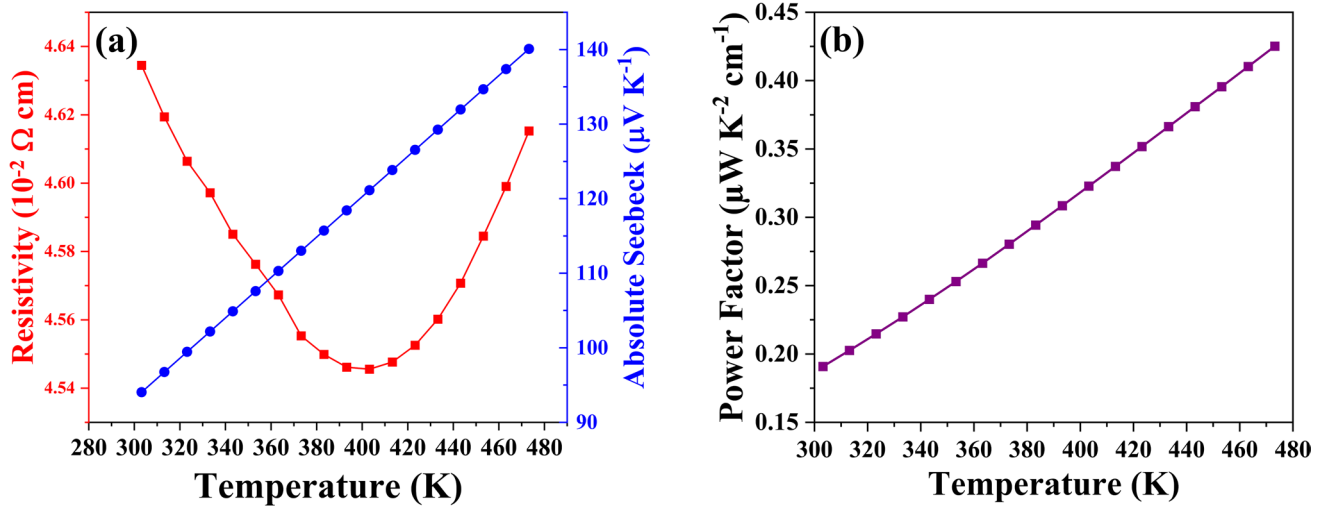


Figure 4 a ρ , S , and b PF for the CTS thin film measured as a function of temperature.

the multiplicative factor in the expression of the Seebeck coefficient:

$$S = A \cdot m^* \cdot \left(\frac{\pi}{3 \cdot n}\right)^{\frac{2}{3}} \cdot T \tag{2}$$

In addition, m^* evolution with temperature as depicted in Fig. 3b proved to be of the same order of magnitude as Zn-doped CTS samples with a similar concentration of charge donors [39], reinforcing the premise of a Cu-poor stoichiometry for this work.

Due to the complex nature of the CTS band structures, the rigid band model (RBM) approximation is the most suitable tool to understand the Seebeck behaviour with carrier concentration. Reports show that for $n = 3.6 \times 10^{20}$, the Seebeck coefficient is about $100 \mu\text{V K}^{-1}$ [6, 31, 33], similar to the present work. Therefore, the unbalanced stoichiometry of the CTS thin films is the main explanation for the reduced Seebeck coefficient, corroborating the fact that the Cu-poor environment observed in our case also acts as a charge carrier donor in the structure.

Snyder et al. [40] introduced a novel approach for determining weighted mobility (μ_w) by using experimentally derived Seebeck coefficient and resistivity data. Their method operates on the premise that charge transport predominantly occurs within a single band. By incorporating a $T^{-3/2}$ term into the μ_w equation of Ref. [40], they noted a consistent decline in μ_w with rising temperature. As observed in Fig. 3b, this suggests that the primary factor influencing the

mobility of charge carriers is the scattering effect induced by acoustic phonons.

Combining the thermoelectric transport properties: electrical resistivity (ρ) or conductivity (σ), and Seebeck coefficient (S), it is possible to evaluate the PF shown in Fig. 4b. Low-density bulk CTS (made with ball-milled powder) revealed a much higher Seebeck coefficient ($\sim 350 \mu\text{V K}^{-1}$) than the present work, resulting in a slightly higher PF [18]. However, when this CTS powder was employed for ink production of the CTS films, the total PF was four times lower than what is reported in the present article [2]. This is especially due to the presence of organic compounds in ink-based techniques, such as oleylamine, used for binding the CTS grains during ink production, acting as charge scatterers between the grains.

Thermoelectric generator

The TEG fabricated with the material above can be characterized by voltage at open-circuit (V_{OC}) measurements and current–voltage–power (I–V–P) curves using the homemade setup described in Sect. 2.3. While applying a temperature gradient (ΔT), the V_{OC} is measured by connecting a voltmeter in parallel to the TEG and applying an infinite (or very high) load resistance in series as shown in Fig. 1c. This way, the highest voltage that can be produced by the device is measured. This kind of measurement reflects the effective Seebeck coefficient of the device. This Seebeck

coefficient is defined as the voltage shift (V_{shift}) due to the thermoelectric effect:

$$V_{shift} = -S(T_h - T_c) \quad (3)$$

where S is the Seebeck coefficient, T_h is the hot side temperature and T_c is the cold side temperature. The films tend to equilibrate the temperature in their extremities during the experiment due to the heat conduction, therefore a Peltier cooler is placed at the cold side, enabling a constant gradient of temperature with time as visible in Fig. 5a. T_c and T_h represent the average temperature values in the area depicted in Fig. 5a.

The V_{OC} vs ΔT plots for the CTS TEGs are shown in Fig. 5b ranging from ~ 50 to 250 K ($T_c = \sim 293$ K). These tests can be used to determine the stability of the device with the temperature, spotted when the behaviour of V_{OC} with ΔT deviates from the linear trend [see Eq. (3)] [15]. Therefore, a second-order polynomial was used for the fitting of the V_{OC} , represented in green in Fig. 5b. This effect is accompanied by the drop in the current measured at zero load resistance, referred to as the short circuit current I_{SC} , also visible in Fig. 5b. Around a ΔT of 250 K, corresponding to a T_h of 550 K, the I_{SC} stabilizes. Therefore, the safe operation T_h temperature for CTS-based TEG is established at around 493 K.

The V_{OC} is similar to the Seebeck measurements performed in the previous section and can be compared to each other. This allows us to infer if the Ag contact deposition provided any decrease in the TE properties. As shown in Fig. 5c, the Seebeck evaluated from the generator is in the order of magnitude of the previously characterized CTS film by the Seebeck option of Fig. 4a. The absolute temperature (T_{abs}) was estimated as an average between T_h and T_c . Therefore, the TE properties of the CTS thin films are not affected by the Ag contact deposition.

To the best of our knowledge, no single CTS thin-film TEG has been reported for performance comparison, except p-n-junctions by Syafiq et al. [2] with the coupling AZO as n -type material and Das et al. [21], coupling CTS with Bi thin films. CTS + AZO revealed a higher V_{OC} voltage compared to our work (~ 98 mV) due to the added p and n -type configuration, similar to CTS + Bi films. On the other hand, the I_{SC} value reported in this study is three times higher compared to the value in Ref. [2], owing to the tenfold increase in electrical conductivity of the evaporated CTS (a comparison made at $\Delta T = 180$ K). In comparison with Ref.

[21], a total of 20 CTS legs were used for the TEG fabrication, revealing higher current and voltage. However, the PF for CTS is orders of magnitude higher in our case, and a normalization per volume of the power generated must be performed in the following for performance comparison.

The I–V curves for the CTS TEG are shown in Fig. 5d for all the ΔT s. The internal resistance ($R = \Delta V / \Delta I$) of the TEG can be calculated from the slope of this curve, with values shown in the inset of Fig. 5d. They are one order of magnitude lower than the ball-milled ink-based thin films reported by Syafiq et al. [2]. CuFeS₂ produced using the same three-step method as developed here [17], also reported a significant drop in resistivity, pointing to the fact that the homogeneity of the films obtained through this method induces a lower overall resistivity. The internal resistance is similar to high-quality sputtered CZTS and CZTSe thin-film materials for a similar film thickness [15]. The P–I plots of the CTS TEGs are shown in Fig. 5e for all the temperature ranges. Since $P = RI^2$, the curve has a characteristic parabolic shape. Intrinsically, the circuit has a built-in resistance, and the maximum of this parabola is obtained when load and built-in resistances are equal. This maximum power (P_{max}) is calculated as $P_{max} = V_{OC}I_{SC}/4$. The results also show that the higher ΔT (and absolute temperature) returns a higher generated power, reaching a maximum of ~ 87 nW for the measured sample at $\Delta T = 250$ K ($T_h = 553$ K). Measurements were repeated three times and showed similar values of P_{max} at each run, confirming the reproducibility of the results at the highest temperature. In addition, two subsequent batches were fabricated using similar conditions of the previous sample and provided slightly different thicknesses of 1.5 , 1.25 , and 1.42 μm for the first, second and third batches of CTS respectively. Their thorough I–V–P characterization is shown in Supplementary Note 2. Normalization of their I–P curves is shown in Fig. 6a for all the batches, demonstrating to be reproducible in terms of maximum power (P_{max}) obtained. Differences in I_{SC} are attributed to slightly different contact resistance of each batch. Furthermore, after the I–V–P characterization of the second and third batches, the films were cooled down and had their performance measured again, as shown in Supplementary Note 2. Each measurement is called a run, and Figure S9 depicts the volume power density for each run. A retrieval of 92 and 76% of the power density from the first and second batches were retrieved, respectively.

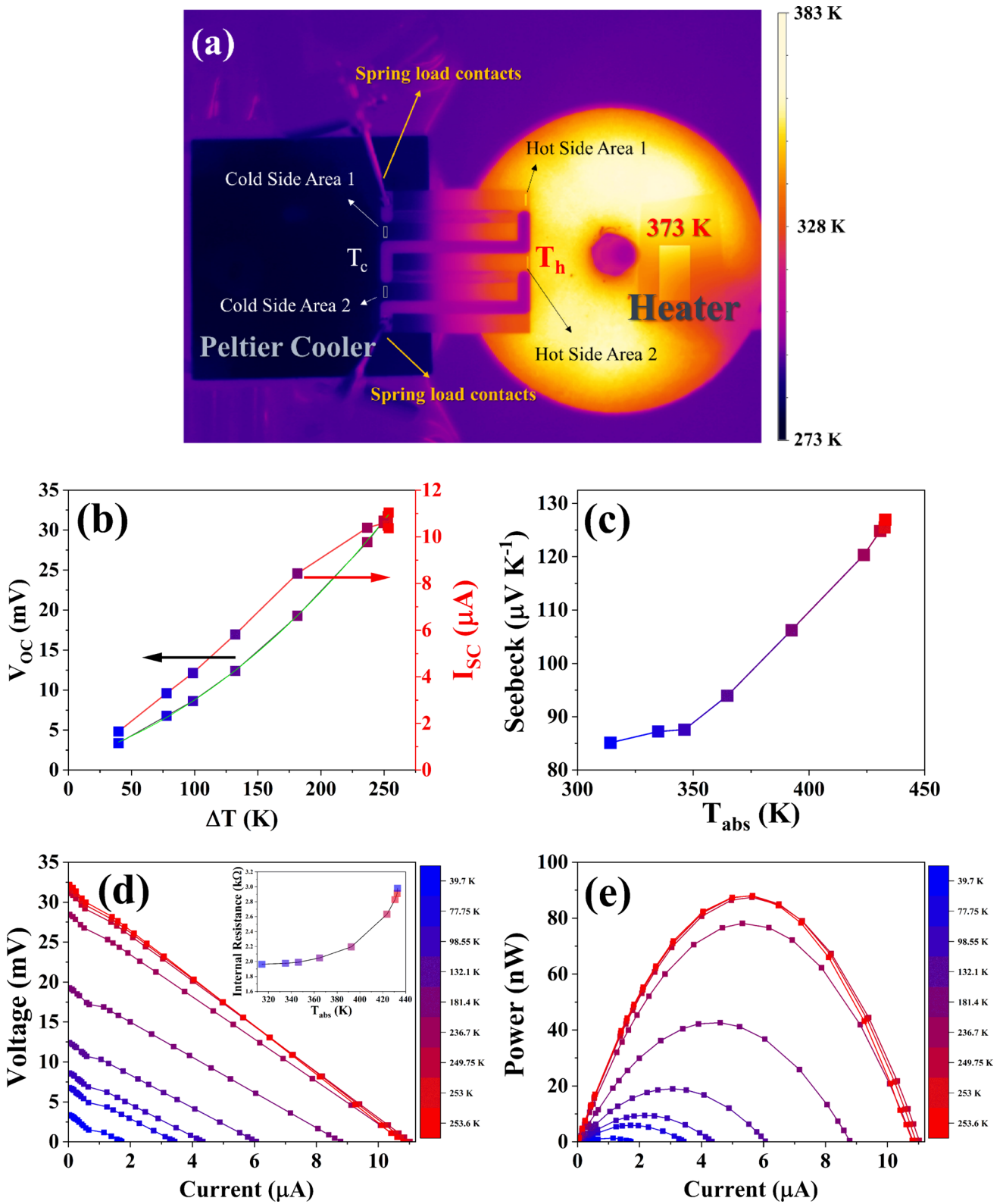


Figure 5 a Infrared image of I–V–P setup during measurement. The top heater was removed for visualization purposes. b V_{OC} and I_{SC} vs gradient of temperature. In green is the second order polynomial fit of the V_{OC} . c Seebeck coefficient vs absolute tem-

perature. d Voltage vs current for the different temperature gradients corresponding to the colour temperature labels. e Power vs current for the temperature gradients corresponding to the colour temperature labels.

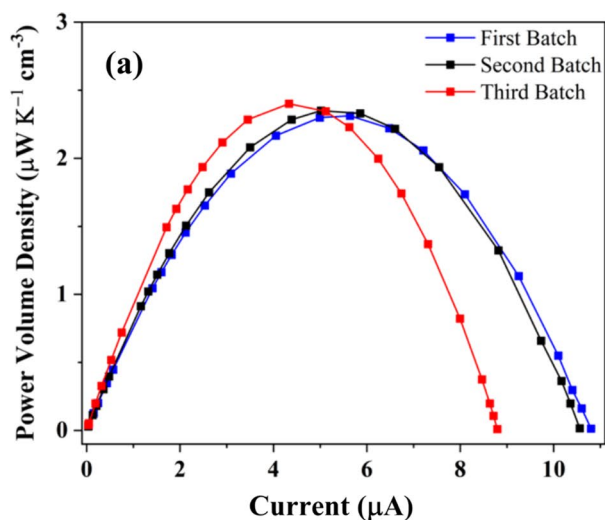
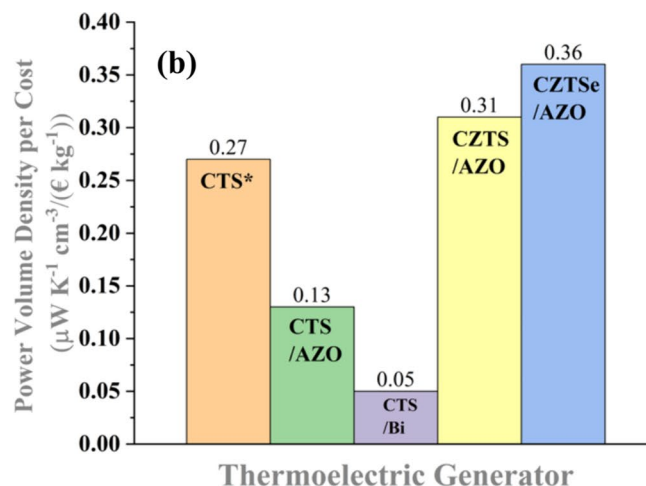


Figure 6 **a** Power volume density of the CTS thin films for different batches. **b** Normalized power volume density per cost of materials for different reports. CTS/AZO represents Ref. [2],



In the literature, TEGs are generally fabricated using different dimensions with the materials employed. Conventionally [15] other normalizations of the maximum power are done by dividing P_{max} by the total area of the device, by the actual area where the TE material is located, or by its cross-sectional area where heat and electricity are conducted. These values are reported in Table 1 for the first batch of CTS thin films, also being divided by the cost of the raw Cu, Sn, and S materials by weight [41–44]. References [2] and [21] employing CTS materials optimized the area production of the TEGs compared to this work. However, from a materials performance perspective, the P_{max} must be normalized by the volume of material for a thorough comparison. Further normalization by the cost of the raw materials is shown in Fig. 6b comparing literature results. An enhancement of 100% in

CTS/Bi Ref. [21], CZTS/ and CZTSe/AZO Ref. [15]. The AZO and Bi areas of the TEGs are not considered in the calculation.

the power volume density compared to ink-based CTS is attributed to the better homogeneity and dry route synthesis of the three-step method, since it does not involve organic materials for the ink, resulting in better electrical contact between CTS grains. In addition, CTS already proved to have a fancy dependence on TE properties due to crystallite size [32] attributed to the enhancement of the TE properties in the grain boundaries, which is facilitated by the three-step method. Compared to the CTS + Bi work [21], produced by the sol-gel technique, we report a five-fold enhancement in the power per unit cost.

Further enhancement of the CTS thin films' electrical properties can be provided using extrinsic doping [5] or by intrinsic doping using a Cu-rich material [33]. This has already been shown to work for Cu-rich CZTS and CZTSe [15] materials produced via sputtering and

Table 1 Maximum power area normalization of the CTS thin film

ΔT	Power per unit area	Power per actual unit area	Power per cross-sectional area	Power density unit area	Cost per raw material	Power density per unit area cost	Power density cross-section area
[K]	[nW cm ⁻²]	[nW cm ⁻²]	[mW cm ⁻²]	[nW K ⁻¹ cm ⁻²]	[€ kg ⁻¹]	[nW K ⁻¹ cm ⁻² / (€ kg ⁻¹)]	10 ⁻⁴ [mW K ⁻¹ cm ⁻² / (€ kg ⁻¹)]
250	14	87	1.45	0.35	8.49	0.041	6.83
180	7	42	0.70	0.23	8.49	0.027	4.58

sulfurization, also compared in Fig. 6b. In this case, density can be further improved by the use of sputtering, however, sputtering also requires the layer deposition of Cu, Zn, and Sn, which has already been shown to be a more complex and expensive procedure when compared to thermal evaporation, also with a lower deposition rate [17].

Other methods are reported in the literature to synthesize CTS through thermal evaporation. Generally, these methods require a previous step of stacking the Cu and Sn layers, where sulphur can be introduced via sulfurization [25, 27]. This procedure is not needed when utilizing a BM pre-step, and in the end, resulted in similar electrical properties to the stacked Cu/Sn methods, providing a simplification of the CTS thin-film fabrication. Another factor of improvement is shown in the three order of magnitude enhancement of the carrier concentration n due to the Cu-poor stoichiometry achieved by the three-step synthesis. Further intrinsic and extrinsic doping can be better controlled via the pre-ball-milling step techniques, which revealed to be the only way to add them in the low quantities required for doping using thermal evaporation.

Conclusion

The three-step synthesis method, involving BM, thermal evaporation, and sulfurization of Cu₂-Sn metallic precursors, successfully produced CTS thin films for TEG fabrication. The combination of factors, including the Cu-poor stoichiometry, which enhanced carrier concentration; and the improved grain boundary connections, resulted in a fourfold increase in the total power factor (PF) and a doubling of the maximum power per volume density compared to the wet chemical methods. Notably, the procedure demonstrated full reproducibility. These results highlight the potential of CTS as a Te-free thermoelectric option, with an evaluated power cost of $0.27 \mu\text{W K}^{-1} \text{cm}^{-3}/(\text{€ kg}^{-1})$; benefiting from its non-toxicity, abundance, and low-cost elemental composition.

Funding

Open access funding provided by Università degli Studi di Trento within the CRUI-CARE Agreement.

This study was funded by the Italian Ministry of Universities and Research (MUR), in the framework of the project DICAM-EXC (Departments of Excellence 2023–2027, grant L232/2016).

Declarations

Conflict of interest The authors declare that they have no conflict of interest.

Supplementary Information The online version contains supplementary material available at <https://doi.org/10.1007/s10853-024-10104-w>.

Open Access This article is licensed under a Creative Commons Attribution 4.0 International License, which permits use, sharing, adaptation, distribution and reproduction in any medium or format, as long as you give appropriate credit to the original author(s) and the source, provide a link to the Creative Commons licence, and indicate if changes were made. The images or other third party material in this article are included in the article's Creative Commons licence, unless indicated otherwise in a credit line to the material. If material is not included in the article's Creative Commons licence and your intended use is not permitted by statutory regulation or exceeds the permitted use, you will need to obtain permission directly from the copyright holder. To view a copy of this licence, visit <http://creativecommons.org/licenses/by/4.0/>.

References

- [1] Finn PA, Asker C, Wan K, Bilotti E, Fenwick O, Nielsen CB (2021) Thermoelectric materials: current status and future challenges. *Front Electron Mater* 1:677845. <https://doi.org/10.3389/femat.2021.677845>
- [2] Syafiq U, Isotta E, Ataollahi N et al (2022) Facile and low-cost fabrication of Cu/Zn/Sn-based ternary and quaternary chalcogenides thermoelectric generators. *ACS Appl Energy Mater* 5:5909–5918. <https://doi.org/10.1021/acsaem.2c00268>
- [3] Zhao Y, Li W, Zhao X, Wang Y, Luo D, Li Y, Ge M (2024) Energy and exergy analysis of a thermoelectric generator system for automotive exhaust waste heat recovery. *App*

- Therm Eng 239:122180. <https://doi.org/10.1016/j.applthermaleng.2023.122180>
- [4] Zaia EW, Gordon MP, Yuan P, Urban JJ (2019) Progress and perspective: soft thermoelectric materials for wearable and internet-of-things applications. *Adv Electron Mater* 5(11):1800823. <https://doi.org/10.1002/aelm.201800823>
- [5] Lohani K, Nautiyal H, Ataollahi N et al (2023) Enhanced thermoelectric performance of nanostructured Cu_2SnS_3 (CTS) via Ag doping. *ACS Appl Nano Mater* 6:6323–6333. <https://doi.org/10.1021/acsanm.3c00716>
- [6] Xi L, Zhang YB, Shi XY et al (2012) Chemical bonding, conductive network, and thermoelectric performance of the ternary semiconductors Cu_2SnX_3 ($X = \text{Se}, \text{S}$) from first principles. *Phys Rev B* 86:155201. <https://doi.org/10.1103/PhysRevB.86.155201>
- [7] Chen X, Zhou Z, Lin YH, Nan C (2020) Thermoelectric thin films: Promising strategies and related mechanism on boosting energy conversion performance. *J Materomics* 6:494–512. <https://doi.org/10.1016/j.jmat.2020.02.008>
- [8] Park NW, Park TH, Ahn JY, Kang SH, Lee WY, Yoon YG, Yoon SG, Lee SK (2016) Thermoelectric characterization and fabrication of nanostructured p -type $\text{Bi}_{0.5}\text{Sb}_{1.5}\text{Te}_3$ and n -type Bi_2Te_3 thin film thermoelectric energy generator with an in-plane planar structure. *AIP Adv* 6(6):065123. <https://doi.org/10.1063/1.4955000>
- [9] Kim SJ, We JH, Cho BJ (2014) A wearable thermoelectric generator fabricated on a glass fabric. *Energy Environ Sci* 7:1959. <https://doi.org/10.1039/c4ee00242c>
- [10] Min G, Rowe DM (1999) Cooling performance of integrated thermoelectric microcooler. *Solid State Electron* 43:923–929. [https://doi.org/10.1016/S0038-1101\(99\)00045-3](https://doi.org/10.1016/S0038-1101(99)00045-3)
- [11] Chen WY, Shi XL, Zou J, Chen ZG (2022) Thermoelectric coolers: progress, challenges, and opportunities. *Small Methods* 6(2):2101235. <https://doi.org/10.1002/smt.202101235>
- [12] Kim M-Y, Oh T-S (2010) Thermoelectric characteristics of the thermopile sensors with variations of the width and the thickness of the electrodeposited bismuth-telluride and antimony-telluride thin films. *Mater Trans* 51:1909–1913. <https://doi.org/10.2320/matertrans.M2010122>
- [13] He J, Li K, Jia L, Zhu Y, Zhang H, Linghu J (2023) Advances in the applications of thermoelectric generators. *Appl Therm Eng* 236:121813. <https://doi.org/10.1016/j.applthermaleng.2023.121813>
- [14] LeBlanc S, Yee SK, Scullin ML et al (2014) Material and manufacturing cost considerations for thermoelectrics. *Renew Sustain Energy Rev* 32:313–327. <https://doi.org/10.1016/j.rser.2013.12.030>
- [15] Isotta E, Andrade-Arvizu J, Syafiq U, Jiménez-Arguijo A, Navarro-Güell A, Guc M, Saucedo E, Scardi P (2022) Towards low cost and sustainable thin film thermoelectric devices based on quaternary chalcogenides. *Adv Funct Mater* 32(32):2202157. <https://doi.org/10.1002/adfm.202202157>
- [16] Mukherjee B, Isotta E, Malagutti MA, Lohani K, Rebuffi L, Fanciulli C, Scardi P (2023) Thermoelectric performance in disordered $\text{Cu}_2\text{ZnSnSe}_4$ nanostructures driven by ultra-low thermal conductivity. *J Alloys Compd* 933:167756. <https://doi.org/10.1016/j.jallcom.2022.167756>
- [17] Malagutti MA, Lohani K, D’Incau M, Nautiyal H, Ataollahi N, Scardi P (2023) Optimizing CuFeS_2 chalcopyrite thin film synthesis: a comprehensive three-step approach using ball-milling, thermal evaporation, and sulfurization applied for thermoelectric generation. *Appl Sci* 13(18):10172. <https://doi.org/10.3390/app131810172>
- [18] Lohani K, Nautiyal H, Ataollahi N et al (2021) Experimental and ab initio study of Cu_2SnS_3 (CTS) polymorphs for thermoelectric applications. *J Phys Chem C* 125:178–188. <https://doi.org/10.1021/acs.jpcc.0c09139>
- [19] Nautiyal H, Lohani K, Mukherjee B et al (2023) Mechanochemical Synthesis of Sustainable Ternary and Quaternary Nanostructured Cu_2SnS_3 , $\text{Cu}_2\text{ZnSnS}_4$, and $\text{Cu}_2\text{ZnSnSe}_4$ chalcogenides for thermoelectric applications. *Nanomaterials* 13:366. <https://doi.org/10.3390/nano13020366>
- [20] Welatta F, El Kissani A, Mellalou A et al (2023) Tuning thermoelectric properties of spin-coated Cu_2SnS_3 thin films by annealing. *J Electron Mater* 52:5396–5400. <https://doi.org/10.1007/s11664-023-10424-8>
- [21] Das S, Mondal BP, Ranjan P, Datta A (2023) High-performance paper-based thermoelectric generator from Cu_2SnS_3 nanocubes and bulk-traced bismuth. *ACS Appl Mater Interf* 15:56022–56033. <https://doi.org/10.1021/acsami.3c13576>
- [22] Chino K, Koike J, Eguchi S, Araki H, Nakamura R, Jimbo K, Katagiri H (2012) Preparation of Cu_2SnS_3 thin films by sulfurization of Cu/Sn stacked precursors. *Jpn J Appl Phys* 51(10S):10NC35. <https://doi.org/10.1143/JJAP.51.10NC35>
- [23] Guo Y-X, Cheng W-J, Jiang J-C, Chu J-H (2016) The effect of substrate temperature, Cu/Sn ratio and post-annealing on the phase-change and properties of Cu_2SnS_3 film deposited by ultrasonic spray pyrolysis. *J Mater Sci: Mater Electron* 27:4636–4646. <https://doi.org/10.1007/s10854-016-4341-8>
- [24] Fernandes PA, Salomé PMP, da Cunha AF (2010) A study of ternary Cu_2SnS_3 and Cu_3SnS_4 thin films prepared by sulfurizing stacked metal precursors. *J Phys D Appl Phys* 43:215403. <https://doi.org/10.1088/0022-3727/43/21/215403>
- [25] Olgar MA, Başol BM, Tomakin M, Bacaksız E (2021) Phase transformation in Cu_2SnS_3 (CTS) thin films through

- pre-treatment in sulfur atmosphere. *J Mater Sci: Mater Electron* 32:10018–10027. <https://doi.org/10.1007/s10854-021-05660-9>
- [26] Dong Y, He J, Li X et al (2015) Synthesis and optimized sulfurization time of Cu_2SnS_3 thin films obtained from stacked metallic precursors for solar cell application. *Mater Lett* 160:468–471. <https://doi.org/10.1016/j.matlet.2015.08.028>
- [27] Ketenci Ozsoy E, Atay F, Buyukgungor O (2021) Production and characterization of Cu_2SnS_3 films for solar cell applications: the effect of the sulfurization temperature on CuS secondary phase. *Sol Energy* 214:179–188. <https://doi.org/10.1016/j.solener.2020.11.068>
- [28] Chaudhari MN, Ahirrao RB, Bagul SD (2021) Thin film deposition methods: a critical review. *Int J Res Appl Sci Eng Technol* 9(6):5215–5232. <https://doi.org/10.22214/ijraset.2021.36154>
- [29] Gates-Rector S, Blanton T (2019) The powder diffraction file: a quality materials characterization database. *Powder Diffr* 34:352–360. <https://doi.org/10.1017/S0885715619000812>
- [30] Coelho AA (2018) TOPAS and TOPAS-Academic: an optimization program integrating computer algebra and crystallographic objects written in C++. *J Appl Crystallogr* 51:210–218. <https://doi.org/10.1107/S1600576718000183>
- [31] Tan Q, Sun W, Li Z, Li JF (2016) Enhanced thermoelectric properties of earth-abundant Cu_2SnS_3 via In doping effect. *J Alloys Compd* 672:558–563. <https://doi.org/10.1016/j.jallcom.2016.02.185>
- [32] Lohani K, Nautiyal H, Ataollahi N et al (2021) Effects of grain size on the thermoelectric properties of Cu_2SnS_3 : an experimental and first-principles study. *ACS Appl Energy Mater* 4:12604–12612. <https://doi.org/10.1021/acsaem.1c02377>
- [33] Deng T, Qiu P, Song Q, et al (2019) Thermoelectric properties of non-stoichiometric $\text{Cu}_{2+x}\text{Sn}_{1-x}\text{S}_3$ compounds. *J Appl Phys* 126(8):085111. <https://doi.org/10.1063/1.5115195>
- [34] Bayazit T, Olgar MA, Küçükömeroğlu T, Bacaksız E, Tomakin M (2019) Growth and characterization of Cu_2SnS_3 (CTS), Cu_2SnSe_3 (CTSe), and $\text{Cu}_2\text{Sn}(\text{S}, \text{Se})_3$ (CTSSe) thin films using dip-coated Cu–Sn precursor. *J Mater Sci: Mater Electron* 30:12612–12618. <https://doi.org/10.1007/s10854-019-01622-4>
- [35] Zhao H, Xu X, Li C et al (2017) Cobalt-doping in Cu_2SnS_3 : enhanced thermoelectric performance by synergy of phase transition and band structure modification. *J Mater Chem A Mater* 5:23267–23275. <https://doi.org/10.1039/c7ta07140j>
- [36] Lohani K, Isotta E, Ataollahi N et al (2020) Ultra-low thermal conductivity and improved thermoelectric performance in disordered nanostructured copper tin sulphide (Cu_2SnS_3 , CTS). *J Alloys Compd* 830:154604. <https://doi.org/10.1016/j.jallcom.2020.154604>
- [37] Adelifard M, Mohagheghi MM, Eshghi H (2012) Preparation and characterization of Cu_2SnS_3 ternary semiconductor nanostructures via the spray pyrolysis technique for photovoltaic applications. *Phys Scr* 85(3):035603. <https://doi.org/10.1088/0031-8949/85/03/035603>
- [38] Lohani K, Fanciulli C, Scardi P (2022) Effects of preparation procedures and porosity on thermoelectric bulk samples of Cu_2SnS_3 (CTS). *Materials* 15:712. <https://doi.org/10.3390/ma15030712>
- [39] Shen Y, Li C, Huang R et al (2016) Eco-friendly *p*-type Cu_2SnS_3 thermoelectric material: crystal structure and transport properties. *Sci Rep* 6:2–9. <https://doi.org/10.1038/srep32501>
- [40] Snyder GJ, Snyder AH, Wood M, Gurunathan R, Snyder BH, Niu C (2020) Weighted mobility. *Adv Mater* 32(25):2001537. <https://doi.org/10.1002/adma.202001537>
- [41] Copper prices per KG/Pound [+Historic Data] Read more at: <https://commodity.com/precious-metals/copper/price/>. Accessed 29 Apr 2024
- [42] Commodities. <https://markets.businessinsider.com/commodities>. Accessed 29 Apr 2024
- [43] Price of sulfur in the United States from 2014 to 2023. <https://www.statista.com/statistics/1031180/us-sulfur-price/>. Accessed 29 Apr 2024
- [44] Selenium Price. <https://www.asianmetal.com/Selenium/>. Accessed 29 Apr 2024

Publisher's Note Springer Nature remains neutral with regard to jurisdictional claims in published maps and institutional affiliations.